A Parametric Study of Erupting Flux Rope Rotation

Modeling the "Cartwheel CME" on 9 April 2008

B. Kliem[1,2,3] · **T. Török**[4,5] · **W. T. Thompson**[6]

Abstract The rotation of erupting filaments in the solar corona is addressed through a parametric simulation study of unstable, rotating flux ropes in bipolar force-free initial equilibrium. The Lorentz force due to the external shear field component and the relaxation of tension in the twisted field are the major contributors to the rotation in this model, while reconnection with the ambient field is of minor importance, due to the field's simple structure. In the low-beta corona, the rotation is not guided by the changing orientation of the vertical field component's polarity inversion line with height. The model yields strong initial rotations which saturate in the corona and differ qualitatively from the profile of rotation *vs.* height obtained in a recent simulation of an eruption without preexisting flux rope. Both major mechanisms writhe the flux rope axis, converting part of the initial twist helicity, and produce rotation profiles which, to a large part, are very similar in a range of shear-twist combinations. A difference lies in the tendency of twist-driven rotation to saturate at lower heights than shear-driven rotation. For parameters characteristic of the source regions of erupting filaments and coronal mass ejections, the shear field is found to be the dominant origin of rotations in the corona and to be required if the rotation reaches angles of order 90 degrees and higher; it dominates even if the twist exceeds the threshold of the helical kink instability. The contributions by shear and twist to the total rotation can be disentangled in the analysis of observations if the rotation and rise profiles are simultaneously compared with model calculations. The resulting twist estimate allows one to judge whether the helical kink instability occurred. This is demonstrated for the erupting promi-

---

[1] Insitut für Physik und Astronomie, Universität Potsdam,
Karl-Liebknecht-Str. 24-25, Potsdam 14476, Germany
email: bkliem@uni-potsdam.de
[2] Mullard Space Science Laboratory, University College
London, Holmbury St. Mary, Dorking, Surrey RH5 6NT, UK
[3] College of Science, George Mason University, 4400
University Drive, Fairfax, VA 22030, USA
[4] LESIA, Observatoire de Paris, CNRS, UPMC, Université
Paris Diderot, 5 place Jules Janssen, 92190 Meudon, France
[5] now at Predictive Science, Inc., 9990 Mesa Rim Road,
Ste. 170, San Diego, CA 92121, USA
[6] Adnet Systems Inc., NASA Goddard Space Flight Center,
Code 671, Greenbelt, MD 20771, USA

nence in the "Cartwheel CME" on 9 April 2008, which has shown a rotation of $\approx 115°$ up to a height of 1.5 $R_\odot$ above the photosphere. Out of a range of initial equilibria which include strongly kink-unstable (twist $\Phi = 5\pi$), weakly kink-unstable ($\Phi = 3.5\pi$), and kink-stable ($\Phi = 2.5\pi$) configurations, only the evolution of the weakly kink-unstable flux rope matches the observations in their entirety.

1. Introduction

The geoeffectiveness of solar coronal mass ejections (CMEs) depends primarily on two parameters, the velocity and the magnetic orientation of the CME at the impact on the Earth's magnetosphere. The higher the CME velocity and the closer its front side magnetic field to a southward orientation, the more intense the interaction will typically be. Therefore, understanding the physics that determines these CME parameters at 1 AU is one of the key issues in space weather research. This involves the formation and main acceleration of the CME in the solar corona, as well as its propagation through the interplanetary space. The particulars of the trigger process also play a role in some events. It appears that typically the corona is the place where the basic decisions are made: will the CME be fast or slow, and will it keep the orientation given by the source, *i.e.*, will its magnetic axis remain oriented nearly parallel to the photospheric polarity inversion line (PIL), or will it rotate substantially?

In the present paper we employ the technique of MHD simulation to carry out a first systematic, but in view of the problem's complexity necessarily incomplete investigation of a number of processes that cause and influence changes of CME orientation in the corona. Such changes can be described as a rotation of the CME volume, more specifically of the magnetic axis of the flux rope in the CME, about the direction of ascent. This *rotation* should be distinguished from the possible rotation of the flux rope about its own axis, referred to as the *roll effect* (Martin, 2003; Panasenco *et al.*, 2011), which we do not address here.

Understanding the rotation of erupting flux ropes in the corona is also relevant for the question which processes trigger the eruptions, as a substantial rotation may indicate the occurrence of the helical kink instability (KI); see, *e.g.*, Rust and Kumar (1996), Romano, Contarino, and Zuccarello (2003), and Rust and LaBonte (2005). This instability is one of the candidate mechanisms for the initiation of CMEs (Sakurai, 1976; Fan and Gibson, 2003; Kliem, Titov, and Török, 2004). It commences when the twist of the rope exceeds a critical value, $\Phi = 2\pi N > \Phi_{\mathrm{cr}}$, where N is the winding number of the field lines about the rope's magnetic axis. The dynamical evolution of the instability has shown very good quantitative agreement with a number of well observed events, which range from confined filament eruptions to the fastest CME on record (Török and Kliem, 2005; Williams *et al.*, 2005). However, Isenberg and Forbes (2007) have pointed out an alternative mechanism for the rotation of line-tied flux ropes, which relies

on the presence of an external toroidal field component, B_{et}, due to sources external to the current in the flux rope and pointing along the rope, *i.e.*, an external shear field component. The mechanism can easily be understood in the simplified picture of a current loop in vacuum field. When the loop legs move out of their equilibrium position to a more vertical orientation, the cross product of the loop current with the shear field component yields a sideways Lorentz force on the legs, which is antisymmetric with respect to the vertical line that passes through the apex of the loop. This torque forces the rising top part of the loop to rotate. The effect is also found in a full fluid description (Lynch *et al.*, 2009). For a given chirality of the erupting field, it yields the same direction of rotation as the helical kink. Hence, a comparative study of these two mechanisms is required before firm conclusions about the occurrence of the KI can be drawn from observations of flux rope rotations, which is a further main objective of this paper.

Since the rotations caused by the KI and by the external shear field point in the same direction, they are difficult to disentangle. In fact, from a more general perspective, they are of similar nature. Both cause a writhing of the flux rope which, by conservation of magnetic helicity, reduces the twist of the rope field lines about the writhing axis. Consequently, one can expect that observed flux rope rotations are often consistent with a range of Φ–B_{et} parameter combinations which give the writhing of the flux rope by the helical kink and by the shear field different individual but similar combined strengths.

Other causes of flux rope rotation include magnetic reconnection with the ambient field (Jacobs *et al.*, 2009; Shiota *et al.*, 2010; Cohen *et al.*, 2010; Thompson, 2011; Vourlidas *et al.*, 2011) and the propagation through the overlying field. The latter comprises any asymmetric deflection of the rising flux from radial ascent, *e.g.*, by adjacent coronal holes (see, *e.g.*, Panasenco *et al.*, 2011), and the interaction with the heliospheric current sheet (Yurchyshyn, 2008; Yurchyshyn, Abramenko, and Tripathi, 2009).

One may conjecture that the generally changing orientation of the PIL with height in the corona acts similarly to the heliospheric current sheet at larger heights, *i.e.*, that the upper part of the rising flux continuously adjusts its orientation to align with the PIL. If this were the dominant effect, the rotation of erupting flux could be predicted rather straightforwardly from extrapolation of the photospheric field, since the overlying field is often close to the potential field. However, this conjecture is not valid in the lower corona where $\beta \ll 1$, and where the main part of the total rotation often occurs. We demonstrate this in the Appendix.

The amount of rotation depends on the individual strengths of the four potentially contributing processes. Each of them is controlled by more than a single parameter. This is immediately obvious for the torque by the shear field, which must depend on the height *profile* $B_{et}(z)$, and for the reconnection, which is sensitive to the *structure* of the ambient field, *i.e.*, whether the field is bipolar, quadrupolar, or multipolar and whether the orientation of the line between the resulting new footpoints of the erupting flux differs strongly from the original orientation. The rotation by the KI does not only depend on the initial flux rope twist, $\Phi - \Phi_{cr}$, but also on the strength and height profile of the overlying field (Török, Berger, and Kliem, 2010). If the overlying field decreases only slowly

with height, then the upward expansion develops slowly and, accordingly, its contribution to the relaxation of the field line tension is initially weak. The relaxation is then primarily accomplished by a strong rotation at small heights. In the opposite case of very strong upward expansion, the rotation is distributed across a large height range, which also increases the likelihood of further changes by the onset of reconnection (see Lugaz *et al.*, 2011 for an example). The effect of the heliospheric current sheet can be expected to depend on the angle with the top section of the flux rope's axis, on the horizontal elongation of the CME (whether its horizontal cross section is very elliptical or more nearly circular), and on the magnetic pressure of the CME relative to the pressure of the interplanetary plasma.

Moreover, the total rotation experienced by an erupting flux rope likely depends also on the dynamics of its evolution. For example, a torque strongly localized at low heights, operating on a still small loop, may hurl the flux around more efficiently than a torque which is distributed across a large height range. As another example, in a complex (multipolar) coronal environment the sequence and strength of reconnection with the ambient field may strongly depend upon the height profiles of the rope's angular and rise velocities caused by other processes, *e.g.*, by an ideal MHD instability. The relative velocity between reconnecting flux systems controls how strongly the reconnection with the ambient field is driven. Hence, quantitative studies of flux rope rotation face a very high degree of complexity.

Here we focus on two mechanisms that can cause strong rotations in the corona, the helical kink instability and the torque exerted by an external shear field component. By comparing a parametric study of both mechanisms in a force-free, line-tied flux rope equilibrium with the data of a well observed, strongly rotating erupting prominence, we demonstrate that their contributions can be disentangled to some degree. We also demonstrate the very strong influence of the ambient potential field's height profile on the amount of rotation by the KI, and briefly address the influence of reconnection between the CME flux rope and the ambient field on the rotation.

This investigation was stimulated by the analysis of the strong rotation in a prominence eruption and CME on 9 April 2008, occasionally referred to as the "Cartwheel CME", in Thompson, Kliem, and Török (2011, in the following Paper I). Their stereoscopic reconstruction revealed the height-rotation profile of the erupting filament/prominence in the core of a CME for the first time (Thompson, Kliem, and Toeroek, 2009). This profile provides a strong constraint for the numerical modeling. In combination with the further observations of the event, it allows us to infer the major causes of the rotation and the range of source parameters compatible with the data. The analysis of Paper I has given the following results relevant for the present study. The prominence erupted from the remnants of NOAA active region (AR) 10989 close to the west limb and appeared as a flux rope – a single, weakly to moderately twisted loop – throughout the height range covered by the STEREO EUVI and COR1 telescopes (Howard *et al.*, 2008), *i.e.*, up to 4 $R_\odot$ from Sun center. It rotated counterclockwise by $\approx 115°$ up to a heliocentric height of 2.5 $R_\odot$, where the rotation leveled off. Two thirds of this rotation were acquired within 0.5 $R_\odot$
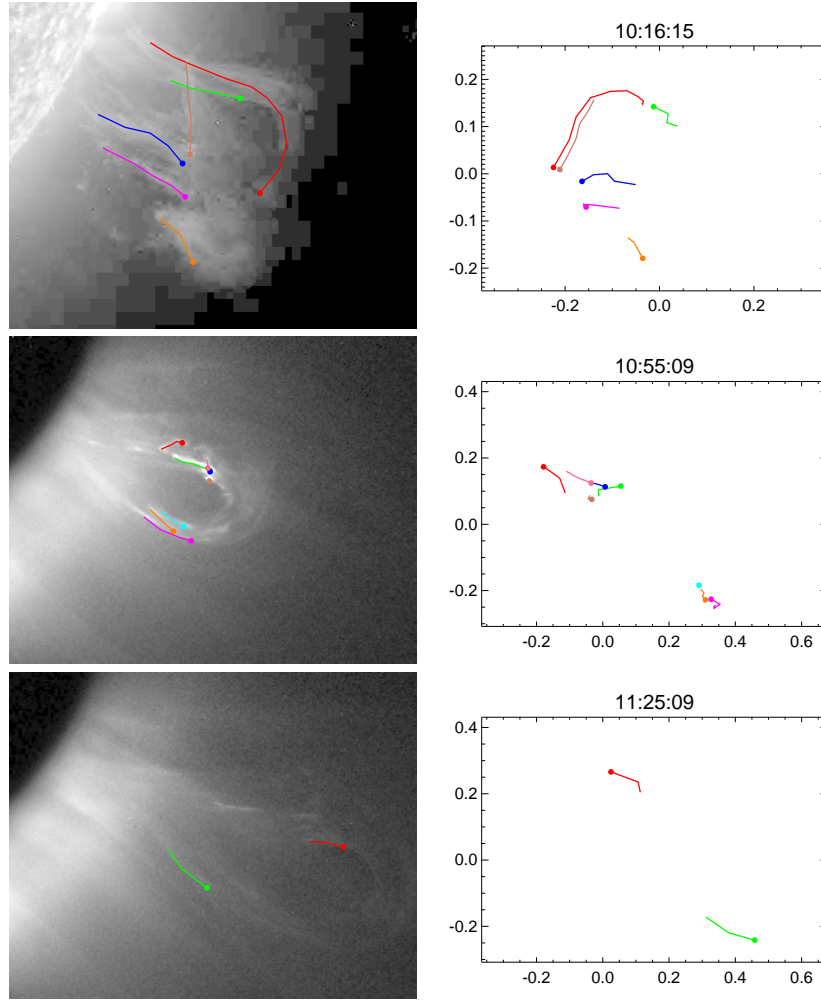
Figure 1. Images and plots of the prominence eruption at 10:16 UT, as seen by the EU-VI-Ahead telescope in the 304 Å channel, and at 10:55 and 11:25 UT, as seen in white light by COR1-Ahead. The prominence apex has reached heights of 0.56, 1.6, and 2.3 $R_\odot$ above the photosphere at these times. The right panels display the reconstructed three-dimensional position of the marked prominence threads, using a reprojection to a viewpoint at the position of radial CME propagation, Stonyhurst longitude 98° west (relative to Earth) and latitude 24° south, where the counterclockwise rotation is apparent. The axes are in units of solar radii.

from the photosphere. The data indicate a subsequent gentle backward rotation by $\approx 15°$ in the height range up to 3.3 $R_\odot$. In addition, the analysis of STEREO COR2 data in Patsourakos and Vourlidas (2011) demonstrated that a flux rope structure is consistent also with the three-dimensional shape of the CME at a heliocentric distance of 13 $R_\odot$, where it had changed its orientation by a total of $150° \pm 7°$ from the original one, most likely by further counterclockwise rotation. At this stage the erupting flux was very closely aligned with the heliospheric

current sheet above the active region. The prominence was initially accelerated mainly horizontally along the filament channel. This gradually turned into a radial propagation at a position ≈ 98W24S as seen from Earth, $15°$–$20°$ away from the original location. The prominence experienced most of its upward acceleration in the heliocentric height range up to $\sim 2.5\ R_\odot$ and reached a velocity of $\sim 400\ \mathrm{km\,s^{-1}}$ in the COR2 field of view. At the same time, the leading edge of the CME accelerated to over $700\ \mathrm{km\,s^{-1}}$ (Landi *et al.*, 2010). Representative images of the prominence from STEREO *Ahead*, which had the best perspective at the structure, and the corresponding three-dimensional reconstructions of the location of several prominence threads are compiled in Figure 1 (from Paper I). The rotation (height-rotation) profile and the rise (time-height) profile are included below in the observation-simulation comparisons (Figures 6 and 8, respectively).

As already noted above, we focus our attention here on the coronal evolution of this event, leaving the interaction with the heliospheric current sheet for future investigation. Moreover, we exclude the possible slight backward rotation by $\approx 15°$ in the COR1 height range from our modeling, since we are interested in the generally important effects which cause significant rotations in the corona. This part of the rotation is not fully certain, and, if real, it was likely caused by the particular structure of the large-scale coronal field above the active region, which nearly reversed its horizontal direction at heights $\gtrsim 0.3\ R_\odot$ above the photosphere (Paper I). Thus, we will consider a saturation of the modeled rotation at angles near $115°$ and heights $h \approx (1.5\text{–}2.3)\ R_\odot$ above the photosphere to be in agreement with the observation data. Furthermore, we will disregard the initial nearly horizontal motion of the prominence along the PIL.

The combined effects of flux dispersal and foreshortening in the course of the source region's rotation to the solar limb made it impossible to obtain a well-defined estimate of the distance between the main flux concentrations in the bipolar region at the time of the eruption, which is a parameter of strong influence on the height profile of the ambient potential field. Only a relatively wide range of $\sim (40\text{–}150)$ Mm could be estimated by extrapolating the region's evolution in the course of its disk passage through the final three days before the event. It will be seen that this range still sets a useful constraint on the modeling.

In the following we model the radial propagation of the prominence in the Cartwheel CME in the coronal range of heights as the MHD evolution of an unstable force-free and line-tied flux rope (Section 2). A parametric study of the resulting rotation and rise, focusing on the rotation caused by the helical kink instability and by the external shear field, is compared with the observation data, to constrain the parameters in the source of the event and to study whether the relative importance of these mechanisms can be disentangled and individually estimated (Section 3). The discussion in Section 4 addresses the simplifying assumptions made in the modeling and differences to earlier relevant work. Section 5 gives our conclusions. The Appendix relates the rotation of erupting flux ropes in low-beta plasma to the changing orientation of the PIL with height.

2. Numerical Model

We carry out a series of MHD simulations similar to the CME simulation in Török and Kliem (2005). The prominence is modeled as a section of an approximately force-free toroidal current channel embedded in external current-free (potential) field, which represents a modification of the approximate force-free equilibrium by Titov and Démoulin (1999). The current channel creates a flux rope structure of the magnetic field which has a somewhat larger cross section than the channel and is enclosed by a quasi-separatrix layer in the interface to the surrounding field of arcade structure. The chirality of the flux rope is chosen to be left handed, so that the rotation will be counterclockwise (Green *et al.*, 2007). The poloidal component of the external field, B_{ep}, is due to a pair of subphotospheric magnetic point sources, which produce a pair of flux concentrations ("sunspots") to the sides of the flux rope (the "prominence") in the magnetogram. This field component holds the current channel in equilibrium; its strength at the position of the rope is exactly proportional to the current in the rope. Consequently, only its spatial profile, determined by the spacing between its sources, can be freely varied. The toroidal component of the external field, B_{et}, is due to a pair of subphotospheric dipoles, positioned under the footpoints of the flux rope such that the field lines of B_{et} run parallel to the magnetic axis of the rope to a very good approximation. Therefore, B_{et} introduces only very minor Lorentz forces in the initial configuration, which quickly decrease by numerical relaxation at the beginning of each run, so that the strength of B_{et} can be chosen freely within a wide range. We will refer to the external toroidal field also as the shear field component. Here it decreases faster with height than the external toroidal field in the original Titov-Démoulin equilibrium. A visualization of the configuration is shown in Figure 2.

We integrate the ideal MHD equations but neglect pressure, as appropriate in the active-region corona, and gravity, because the hydrostatic pressure profile along the field is not essential for the flux rope rotation, which is driven by the Lorentz force. These simplifications yield maximum freedom in the scalability of the simulation results to the data. Magnetic reconnection can occur due to the numerical diffusion of the field in regions of strong gradients. The initial density is specified as $\rho_0(\mathbf{x}) = |\mathbf{B}_0(\mathbf{x})|^{3/2}$, where $\mathbf{B}_0(\mathbf{x})$ is the initial magnetic field. This yields a slow decrease of the Alfvén velocity with height, as in the corona. The box is a cube 64 units long on each side, significantly larger than in our previous simulations and in each direction at least twice as large as the biggest size of the structures that will be compared to the data. It is resolved by a nonuniform, fixed Cartesian grid with a resolution of 0.04 units in the central part of the box (a factor of 2 coarser than in Török and Kliem, 2005). Rigid boundary conditions are implemented at the top and side boundaries, while very small velocities are permitted in the bottom boundary. Initially the torus lies in the plane $\{x = 0\}$. The MHD variables are normalized by the initial apex height of the flux rope axis, h_0, by the initial field strength B_0, density ρ_0, and Alfvén velocity V_{A0} at this point, and by the corresponding quantities derived thereof, *e.g.*, the Alfvén time $\tau_A = h_0/V_{\mathrm{A0}}$. Thus, the initial apex height of the axis of the current channel and flux rope serves as the length unit.

The parameters of the initial configuration are largely chosen as in Török and Kliem (2005). We fix the major radius of the torus at $R = 1.83$, the depth of the torus center at $d = 0.83$ and the pre-normalization strength of the point sources at $q = 10^{14}$ Tm^2 in all runs. For a base set of the simulation series, discussed below in Figures 3–6 and 8–9, we further fix the distance of the point sources from the z axis at $L = 0.83$ (in units normalized such that h_0 is unity). This value lies in the middle of the estimated range for the corresponding distance of the flux concentrations in AR 10989, given above, when the scaling $h_0 = 0.077\, R_\odot$ adopted in Section 3.1 is applied. It also agrees with the settings in several previous investigations (*e.g.*, Török and Kliem, 2005; Török, Berger, and Kliem, 2010), facilitating comparisons. Variations of this parameter will be considered in the range $L = 0.42$–2.5. We vary the minor radius of the toroidal current channel, $a = 0.32$–0.62, and the strength of the external toroidal field, $B_{\mathrm{et}}/B_{\mathrm{ep}} = 0$–1.06 at the flux rope apex $\mathbf{x} = (0, 0, 1)$, to obtain a range of values for the average twist of the current channel, $\Phi = (2.5$–5.0$)\pi$, and for the strength of the shear field component. The twist is influenced by both a and B_{et}, with a having the stronger influence within the considered range of parameters. The twist values quoted in this paper represent the initial twist averaged over the cross section of the current channel in the manner described in Török, Kliem, and Titov (2004).

The range of the initial average twist is chosen such that unstable and stable configurations with respect to the helical kink mode are included. The first group is unstable from the beginning of the simulation. Nevertheless, a small upward initial velocity perturbation is applied in the vicinity of the flux rope apex (typically ramped up to $0.05\, V_{\mathrm{A0}}$ over $5\, \tau_A$ and then switched off), to ensure that the instability displaces the apex upwards, *i.e.*, downward kinking is excluded in these runs which are intended to model CMEs.

For the geometric parameters of the system specified above, the flux rope is initially stable with respect to the torus instability (Kliem and Török, 2006; Török and Kliem, 2007). However, the helical kink instability lifts the rope into the torus-unstable range of heights $(h \gtrsim 2\, h_0)$, from where the torus instability accelerates its top part further upwards.[1] The kink-stable cases require that the upward velocity perturbation is applied for a longer time, lifting the apex into the torus-unstable range. This allows us to study the influence of the shear field on the rotation in the absence of the helical kink instability, using uniform geometrical parameters of the initial flux rope (except for the minor flux rope radius a) in all runs. An initial velocity perturbation very close to the required minimum value is applied in each of these cases, to ensure nearly uniform conditions at the onset of the instability throughout the series. The values at the end of the ramp phase stay below $0.12\, V_{\mathrm{A0}}$ for all runs. The flux rope velocity falls back to a much smaller value (typically $\approx 0.01\, V_{\mathrm{A0}}$) immediately after the perturbation is switched off. The growing instabilities then accelerate the apex to peak upward velocities in the range $\max\{u_{\mathrm{a}}\} \approx (0.4$–0.7$)\, V_{\mathrm{A0}}$, far higher than the initial perturbation.

---

[1]The torus instability can be considered as a lateral kink of the current channel. However, we choose "kink" and "KI" to refer exclusively to the helical kink mode in this paper.
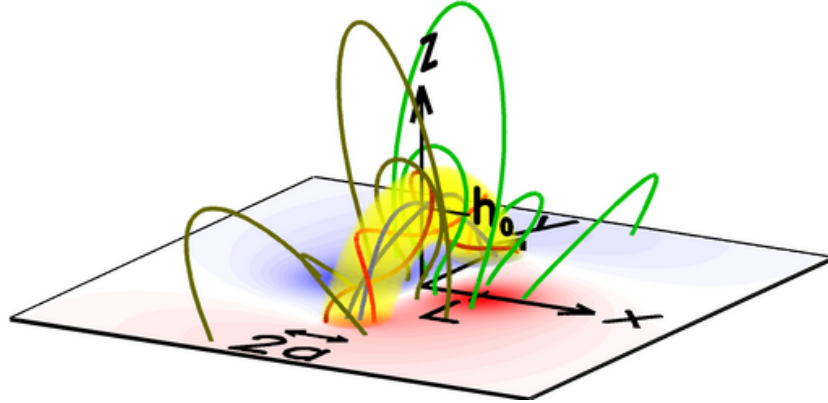
Figure 2. Visualization of the modified Titov-Démoulin flux rope equilibrium used as the initial condition in the simulation runs of this paper; here with an average twist $\Phi = 3.5\pi$ as in Figure 4. The current channel is rendered as a yellow transparent volume. Blue field lines run near the magnetic axis of the flux rope (where the local twist is 2π), red field lines lie in the flux surface at a distance to the axis where the local twist equals the average twist. Green and olive field lines show the ambient potential field. Contours of the magnetogram, $B_z(x, y, 0)$, are shown in the bottom plane. The torus of major radius R and minor radius a is submerged by a distance d, resulting in the apex height $h_0 = R - d$ and the distance of each flux rope footpoint from the origin $D_f = (R^2 - d^2)^{1/2}$. A bipole, whose components are located at $(\pm L, 0, -d)$, is the source of the external poloidal field component B_{ep}; see Figure 2 in Titov and Démoulin (1999) for its visualization. A pair of antiparallel, vertically oriented dipoles, placed under the footpoints of the flux rope at $(0, \pm D_f, -5h_0)$, provides the source of the external toroidal (shear) field component B_{et}.

On the Sun, the initial lifting of the flux can occur by a variety of effects in addition to the helical kink mode, as has been demonstrated by numerical simulations. These include the shearing and twisting of the coronal field by photospheric flows (*e.g.*, Mikic and Linker, 1994; Török and Kliem, 2003), reconnection associated with flux cancellation in the photosphere (*e.g.*, Aulanier *et al.*, 2010; Amari *et al.*, 2010), and reconnection with newly emerging flux (Chen and Shibata, 2000).

The observations of the Cartwheel event indicate a gradual doubling of the prominence height prior to the eruption (Paper I). The initial lifting of the flux rope apex in the simulations due to the applied perturbation is much smaller for all kink-unstable runs and stays in the range up to this value for the kink-stable cases, except for the run with the highest shear field ($\Phi = 2.5\pi$, $B_{et}/B_{ep} = 1.06$), which requires a lifting to $2.6\ h_0$.

3. Comparison Simulations-Observations

### 3.1. Dependence of Flux Rope Rotation on Twist and Shear

We begin with a case that involves a clear helical kink instability, as one would expect at first sight from the considerable rotation observed in the Cartwheel event.

The initial average twist is chosen to be $\Phi = 5\pi$, a value used previously in the successful modeling of several filament/prominence eruptions (Williams *et al.*, 2005; Török and Kliem, 2005). Even with this considerable amount of twist (and with the sunspot semi-distance $L = 0.83$), we find that a shear field is required to reach the observed rotation. Figure 3 shows the resulting rotation of the flux rope, which reaches the observed value of $115°$ and is a combined effect of the helical kink instability and the shear field. The field lines visualize a flux bundle in the core of the rope which runs slightly ($\approx 5\%$) under the rope axis in its top part. This is a likely location for prominence material within a flux rope. Moreover, this is the only selection that allows a favorable comparison with the observed flux rope shape for the weakly twisted case shown below in Figure 5, while the more strongly twisted cases are less sensitive to this vertical offset. Therefore, we adopt this selection as a uniform choice for Figures 3-5 which compare the flux rope rotation for different twist values. The field lines are displayed from perspectives identical to the STEREO images and reconstructions in Figure 1.

Two characteristic morphological features apparent in the COR1 data in Figure 1 are weakly indicated in the simulation: the initial teardrop-like appearance and the elongated shape at large heights (relatively narrow in the horizontal direction). The right panels show that the teardrop shape is a projection effect. The legs of the erupting rope approach each other near the edge of the occulting disk only in projection; they are displaced along the line of sight and actually moving away from each other. The elongated shape is largely also due to the strong rotation.

The legs of the rope appear "wiggly", which results from two effects. First, they reconnect with the ambient field in the vertical current sheet under the flux rope apex in the interval $t \approx (32\text{--}65)\,\tau_A$, which corresponds to apex heights $h \approx (5\text{--}21)\,h_0$; with the reconnection proceeding at much lower heights inside the edge of the COR1 occulting disk. This leads to a bend in the reconnected flux rope: the field lines have relatively small curvature within the legs of the expanded original rope above the reconnection point but run along a more helical path in the ambient field just outside the original rope below the reconnection point. This bend and the more helical shape of the field lines below it relax upward, along with the overall upward expansion of the reconnected flux rope. Since the flux rope apex has reached a considerable upward velocity, $u_a \lesssim 0.5\,V_A$, the bend needs a large height range for its propagation to the top of the rope. It is located slightly above the dotted line in the third snapshot pair of Figure 3 and at $h \gtrsim 15\,h_0$ in the final snapshot pair. The plots on the right hand side show that the new footpoints of the rope are displaced in counterclockwise direction from the original ones, thus contributing to the overall counterclockwise rotation of the rope. However, this contribution is only a minor one; the major part of the total rotation occurs before the flux rope legs reconnect (which can be seen by comparison with Figure 6 below). This reconnection is similar to the second and third reconnections described in Gibson and Fan (2008, their Section 4.1) and will be addressed in more detail in a future investigation. Second, at the given relatively high value of the twist, the dominant wavelength of the helical kink mode is considerably shorter than the flux rope, so that the characteristic helical shape develops clearly.
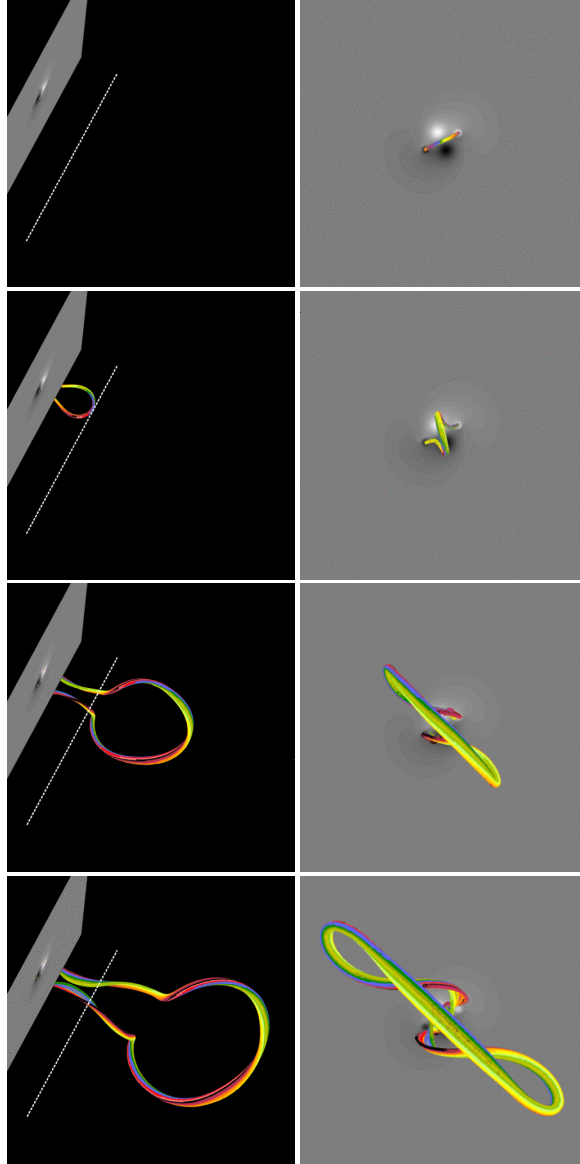
Figure 3. Snapshots of an erupting and rotating, strongly kink-unstable flux rope. The initial average twist is $\Phi = 5\pi$ and the shear field component at the initial flux rope apex position is given by $B_{\mathrm{et}}/B_{\mathrm{ep}} = 0.42$. Field lines in the core of the rope, traced downward from the apex, are shown in the height range $0 \leq z \lesssim 30$, using the same two perspectives as for the observation data in Figure 1 (in the left panels the line of sight makes an angle of $26°$ with the y axis, and the z axis is tilted away from the observer by $8°$, while the right panels present a vertical view with an initial angle between the flux rope axis and the east-west direction of $26°$). The magnetogram, $B_z(x, y, 0, t)$, is displayed in grayscale (seen from below in the left panels). The dotted line indicates where the edge of the COR1 occulting disk is located if the distance between the flux rope footpoints in the simulation, $2D_{\mathrm{f}} = 3.3\ h_0$, is scaled to the value of 175 Mm estimated in Paper I. Using this scaling, the simulated heights of $h = 1, 7.3,$ 21, and 30 h_0 (at $t = 0, 36, 64,$ and 84 τ_A) translate to heights of 0.077, 0.56, 1.6, and 2.3 $R_\odot$ above the photosphere, reached at 10:16, 10:55, and 11:25 UT (for rows 2–4), respectively.
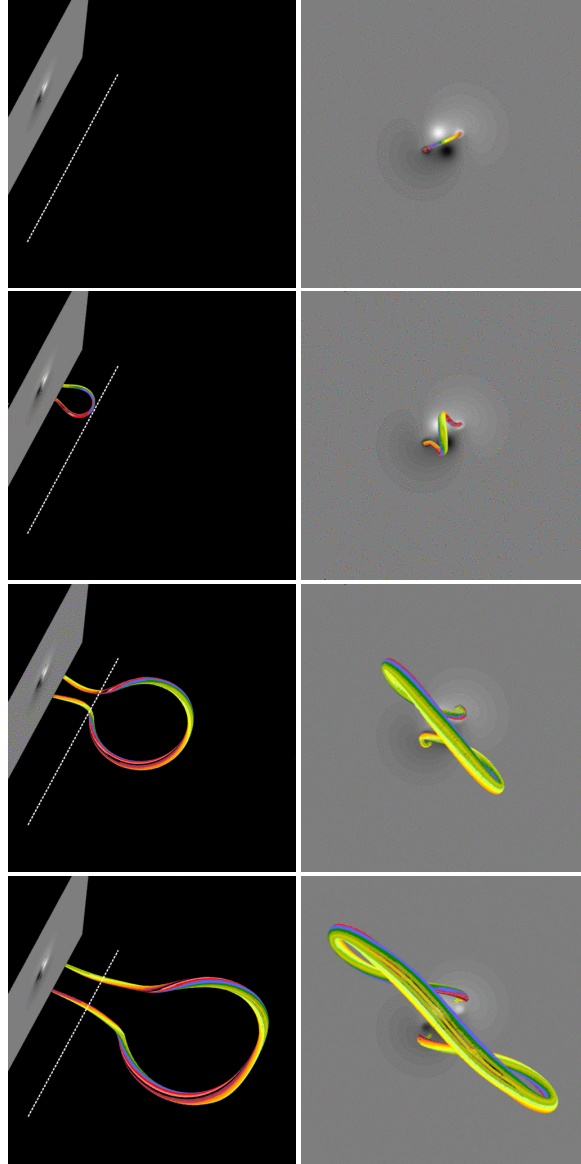
Figure 4. Same as Figure 3 for a weakly kink-unstable case with initial avarage twist $\Phi = 3.5\pi$ and shear field $B_{\mathrm{et}}/B_{\mathrm{ep}} = 0.67$. The flux rope is shown at the simulation times $t = 0, 50, 80$, and 97 τ_A which yield the same heights as the snapshots in Figure 3, corresponding to the same observation times.
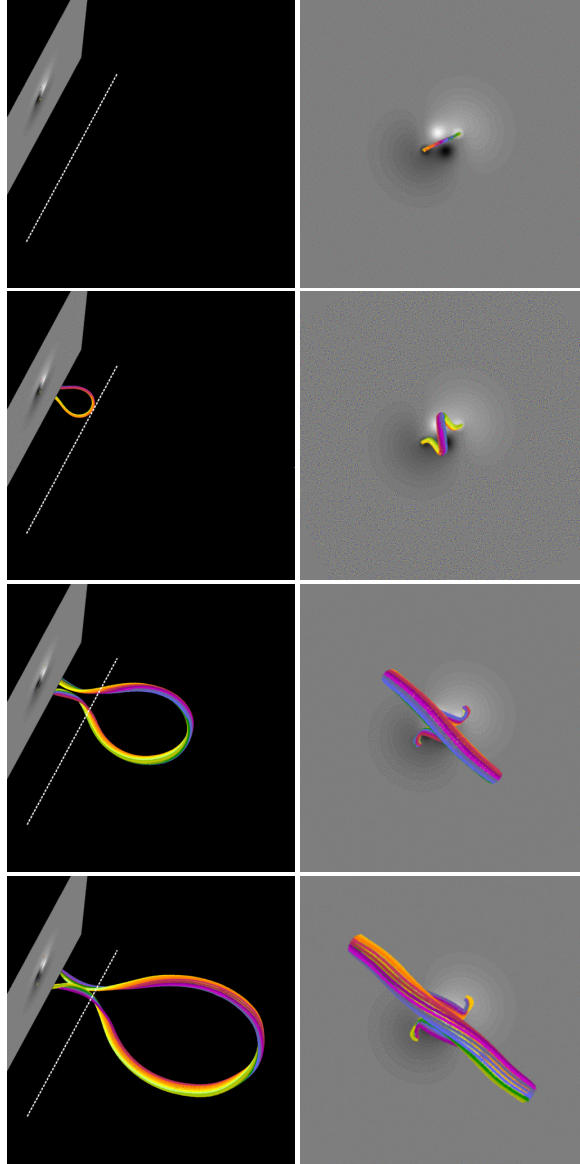
Figure 5. Same as Figure 3 for a kink-stable case with initial avarage twist $\Phi = 2.5\pi$ and shear field $B_{\mathrm{et}}/B_{\mathrm{ep}} = 1.06$. The flux rope is shown at the simulation times $t = 0$, 77, 109, and 128 τ_A which yield the same heights as the snapshots in Figure 3, corresponding to the same observation times.

Figure 4 shows the evolution in a second run where the KI develops only weakly, using a moderate, only slightly supercritical value of the initial average twist, $\Phi = 3.5\pi$. A stronger shear field is chosen, so that the same total rotation is achieved. The overall properties – accelerated rise into an ejection (CME) and very strong rotation – are identical to the run shown in Figure 3. The morphological details, such as the teardrop shape at small heights and the elongated shape at large heights, match the data slightly better. The indications of wiggly shape at large heights remain weak. Reconnection of the flux rope legs with the ambient field occurs here as well, but the resulting changes in the shape of the flux rope are weaker, since not only the field lines in the rope are less twisted but also the ambient field is less helical, due to the larger B_{et}. This morphological difference to the strongly twisted flux rope is one aspect that may allow to distinguish between rotations with strong and weak involvement of the helical kink in observed events. The field line shapes in the present case conform slightly better to the inclination of the prominence threads with respect to the axis of the flux rope in the COR1 data in Figure 1, but this difference is not sufficiently clear to be decisive by itself. Moreover, it depends to a considerable degree upon which part of the erupting flux was outlined by prominence material in the considered event and on the selection of field lines in the plots.

Figure 5 presents a case with subcritical flux rope twist, $\Phi = 2.5\pi$, where the kink instability cannot develop and an even stronger shear field is needed to achieve a similar rotation. Here the parameters were chosen such that the rotation matches the observations as well as the other two runs in the height range $h \lesssim 20\ h_0$, with the total rotation of the rope's magnetic axis at $h = 30\ h_0$ exceeding the rotation in those runs by 20–25 degrees. The elongated teardrop shape at intermediate and large heights yields the best match of the three runs shown in Figures 3–5. However, this is only the case because a flux bundle slightly under the magnetic axis of the flux rope is selected in the visualization. If instead a set of field lines encircling the flux rope axis is chosen, then the high total rotation at the apex height $h = 30\ h_0$ leads to an inverse teardrop shape (narrow at the apex, because at this point the view is nearly along the axis of the rotated flux rope), which is inconsistent with the observations. Again, since it is not known which parts of the erupting flux (rope) were filled with prominence material in the event to be modeled, these morphological comparisons, by themselves, do not allow to rule out the kink-stable run shown in Figure 5.

The similar total rotations in the three simulations confirm that both twist and shear belong to the key parameters which determine the amount of rotation in erupting flux ropes. To analyze this further, we consider a set of characteristic cases from our series of simulation runs with varying strength of the two effects. For each of the twist values $\Phi = 5.0$, 3.5, and 2.5π, we vary the shear field B_{et} from the respective best fitting value used in Figures 3–5. All runs use the same sunspot semi-distance $L = 0.83$ and, hence, the same external poloidal field B_{ep}. The variation of L will be considered in Section 3.2.

The rotation of the flux rope in the simulations is measured in two ways. At low heights it is taken from the changing orientation of the magnetic axis at the apex of the flux rope. As the flux rope rises, the apex orientation oscillates increasingly, due to the upward propagation of Alfvénic perturbations which

result from the dynamic onset of reconnection in the vertical current sheet under the rope (the relaxation of the bend in the reconnected field lines mentioned above). The right panels at the two final heights in Figures 4–5 indicate the resulting oscillations of the field orientation at the apex with respect to the bulk orientation of the flux rope's upper part. Therefore, at larger heights we simply use the direction of the horizontal line connecting the flux rope legs at the height where they are most distant from each other. This measurement filters away most of the oscillating variations, which are also not captured by the observed rotation data derived in Paper I and replotted in Figure 6. The difference between the two measurements remains less than 5 percent in a height range $\Delta h \sim (3\text{–}6)\ h_0$ around $h \sim 10\ h_0$, except for the most strongly rotating and oscillating case in the series ($\Phi = 5\pi$, $B_{\mathrm{et}}/B_{\mathrm{ep}} = 0.63$) where it reaches ≈ 10 percent. Linear interpolation between the two measurements for each simulation run is applied in the appropriate range of small difference to match them smoothly. (The method to estimate the rotation angle at large heights fails for one of the runs in Figure 6 ($\Phi = 2.5\pi$, $B_{\mathrm{et}} = 0$), where reconnection of the flux rope legs with the ambient field leads to jumps that are larger than the oscillations of the magnetic axis at the apex. For this run, whose rotation profile differs strongly from the observed one, we include the rotation angle only at low heights, to show the trend.)

In order to compare the simulated rotation profiles with the observations, a scaling of the length unit in the simulations to distances on the Sun is required. For this purpose, we set the distance between the footpoints of the flux rope in the simulation, $2D_{\mathrm{f}} = 3.3\ h_0$, equal to the estimated length of the flux which holds the prominence, 175 Mm (Paper I). This is independent of the actual prominence shape. The apex height of the toroidal Titov-Démoulin flux rope, our length unit, tends to be somewhat high in comparison to solar prominences, which are often quite flat. Here we obtain $h_0 = 0.077\ R_\odot$, relatively close to the estimated initial prominence height of $\approx (0.05\text{–}0.06)\ R_\odot$ (Paper I). If we would instead choose to compare the simulations to the temporal profile of the prominence rotation, then each change of the twist, which implies a change of the KI growth rate, would require a rescaling of the time unit in the simulations, τ_A. The comparison of the simulated rotation profiles with the observed profile is displayed in Figure 6. As discussed in Sections 1 and 4, we disregard the slight backward rotation at $h \gtrsim 1.5\ R_\odot$ above the photosphere in the comparison and assume that the tendency of the rotation to level off at this height would have continued in the absence of the specific complex structure of the large-scale coronal field above AR 10989 and in the absence of the heliospheric current sheet, which are not included in our model. Several conclusions can be drawn from this set of simulations.

(1) Similar height-rotation profiles (not only a similar total rotation) are obtained in a range of Φ-B_{et} combinations. The profiles for $(\Phi, B_{\mathrm{et}}/B_{\mathrm{ep}}) = (5\pi, 0.42)$, $(3.5\pi, 0.67)$, and $(2.5\pi, 1.06)$ all match the observed profile very well up to a height $h \sim 20\ h_0 \approx 1.5\ R_\odot$ above the photosphere, where a total rotation of $\approx 115°$ is observed. These runs include a strongly and a weakly kink-unstable and a kink-stable case. Hence, even such a strong rotation does not by itself imply the occurrence of the helical kink instability. Further arguments, such as

those given below, are required to draw conclusions about the occurrence of the instability in the modeled event.

(2) To reach the observed total rotation of $\approx 115°$ with the initial configuration and parameter settings chosen in this series, in particular with the chosen value of the sunspot semi-distance L, the shear must contribute. The strongly twisted configuration ($\Phi = 5\pi$) yields only little more than one third of the observed rotation in the absence of shear ($B_{et} = 0$). Therefore, the shear contributes the main part of the total rotation even in this strongly kink-unstable case. Note that this conclusion changes if the sunspot distance is set to larger (however, unrealistic) values, so that the overlying field decreases less steeply with height (see Section 3.2).

(3) The twist also contributes in all runs. The tension of the twisted field relaxes in any case when the flux rope is driven upward out of its initial equilibrium, be it by the helical kink instability, by the torus instability, or by any other process (*e.g.*, by so-called tether-cutting reconnection). This relaxation contributes to the writhing of the flux rope axis regardless of whether or not the helical kink instability is triggered. As a consequence, we do not observe a jump in the achieved rotation as the twist of the initial equilibrium is varied between kink-stable and kink-unstable values. This is most obvious from the runs with $B_{et} = 0$.

(4) The higher the relative contribution of the twist, the lower the height range where most of the rotation is reached. This reflects the fact that the KI tends to reach saturation quickly, often already when the flux rope has risen to a height comparable to the footpoint distance (*e.g.*, Török, Kliem, and Titov, 2004). This property corresponds well to the tendency of the rotation to level off at the relatively low height of $\approx 1.5~R_\odot$ ($\approx 20~h_0$) above the photosphere. The rotation by the shear field acts in a larger height range. The different behavior can be made plausible from the fact that the Lorentz force due to the shear field depends on the current through the rope and on the angle between the flux rope legs and the shear field. While the current decreases as the rope ascends (similar to the twist), the angle rises until the legs approach a vertical position, which corresponds to bigger apex heights than the saturation height of the helical kink mode. Hence, the Lorentz force due to the shear field acts strongly in a larger height range than the tension force associated with the twist.

As a consequence, the Titov-Démoulin flux rope with sub-critical twist for KI onset does not allow to match the entire observed rotation profile of the 9 April 2008 event. We have performed considerable numerical experimenting in this range of twists [$\Phi = (2.5–3)\pi$], including modifications of the height profiles $B_{et}(z)$ and $B_{ep}(z)$ and of the flux rope shape (by varying its major radius R but not the apex height h_0) from the uniform settings for the runs in Figure 6. Either the rotation in the height range $h \lesssim 20~h_0$ was found to be too small, or the total rotation at $h = 30~h_0$ was too large. Although the shape of the prominence in the plane of the sky can still be met by the special selection of the field lines in Figure 5, the saturation of the rotation at $h \approx 1.5~R_\odot$, revealed by the stereoscopic reconstruction, cannot be reproduced. This suggests that at least a weak helical kink instability must have been triggered in this event.
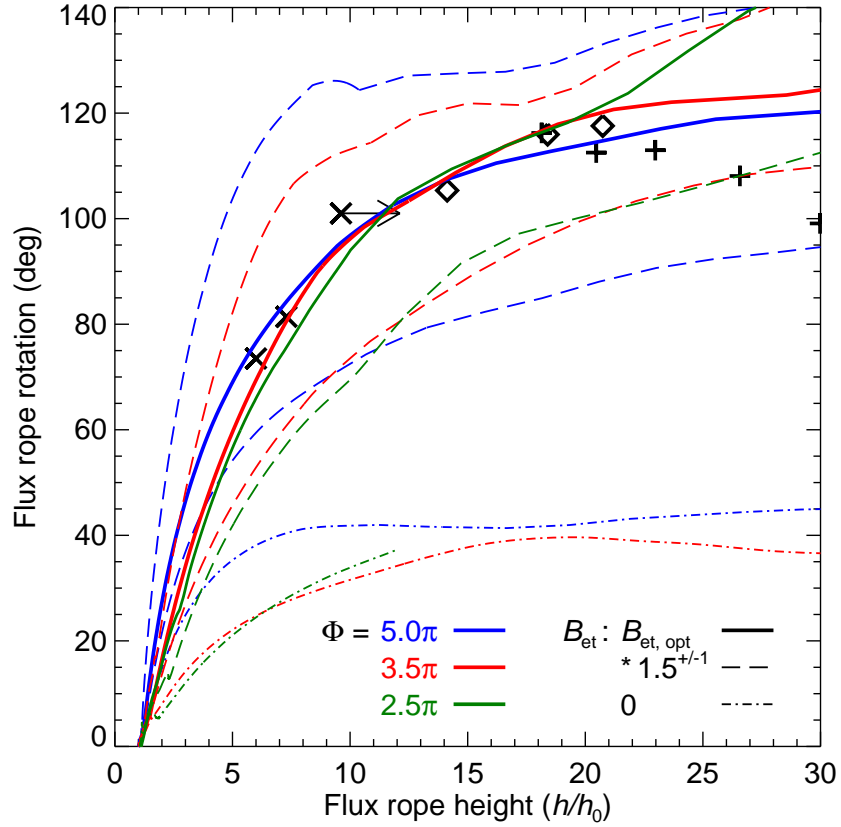
Figure 6. Comparison of flux rope rotation as a function of normalized apex height above the photosphere with the observation data obtained in Paper I. Crosses and diamonds are EUVI data, with the final cross representing a lower limit for the height and the diamonds representing interpolated heights. Plus symbols are COR1 data. The distance between the footpoints of the flux rope in the simulation is scaled to the value of 175 Mm estimated in Paper I, resulting in $h_0 = 0.077 \ R_\odot$. The initial average twist, Φ, and the strength of the shear field component (external toroidal field), B_{et}, given by its ratio to the external poloidal field component B_{ep} at the initial flux rope apex, are varied, while the geometrical parameters of the initial flux rope (except the minor radius a) and the spatial structure of the external field components B_{et} and B_{ep} are uniformly chosen throughout the series of runs (see Section 2 for detail). The optimum values for the shear field strength, which yield the best match with the observed rotation profile up to $h \approx 20 \ h_0$, found through parametric search, are $B_{et, \, opt}/B_{ep} = 0.42$, 0.67, and 1.06 for $\Phi = 5.0\pi$, 3.5π, and 2.5π, respectively. Changes of B_{et} by a factor $3/2$ and the case $B_{et} = 0$ are included.

(5) The range of twist-shear combinations that reproduce the observed rotation profile is bounded not only from below, as outlined in (2) and (4), but also from above. Average twists significantly exceeding 5π are not only unlikely to occur in the corona but also lead to increasingly strong helical deformations of the flux rope, which are favorable for the onset of magnetic reconnection with the overlying field or between the flux rope legs. Such reconnection can strongly distort the rotation profile and can even stop the rise of the flux rope (Török and Kliem, 2005; Shiota *et al.*, 2010). Reconnection with the overlying

field does indeed lead to a confined (failed) eruption in the present simulation series when the initial twist is raised to 6π. Reconnection between the legs of the rope occurs if $\Phi \geq 7\pi$, also leading to confined eruptions. (A detailed description of such reconnection can be found in Kliem *et al.*, 2010.)

Increasing the shear field tends to stabilize the flux rope because any displacement then requires an increasing amount of energy to push the ambient field aside. The low-twist case ($\Phi = 2.5\pi$) with the strongest shear field included in Figure 6 requires a considerable initial perturbation to reach the torus-unstable range of heights ($h > 2.6\ h_0 = 0.2\ R_\odot$ for these parameters); it is completely stable to small perturbations. Similarly, while the 3.5π run with $B_{et} = 0$ is clearly kink-unstable, the corresponding sheared case ($B_{et}/B_{ep} = 0.67$) exceeds the instability threshold only slightly. The initial lifting of the flux rope required in the low-twist case strongly exceeds the observed rise of the prominence to $\approx 0.06\ R_\odot$ prior to the onset of the eruption. This represents a further strong indication against this configuration.

The upper limit for the shear field is not a universal number but depends on other parameters of the system, which include the thickness of the flux rope, the strength of the line tying, and the height profile of the external poloidal field, $B_{ep}(z)$. A systematic study of these dependencies would be beyond the scope of the present investigation. However, we have considered a change of the height profile $B_{ep}(z)$, which is the key parameter for the onset of the torus instability in the absence of shear and significant line tying (Kliem and Török, 2006). In an attempt to ease the occurrence of the instability in the low-twist case ($\Phi = 2.5\pi$, $B_{et}/B_{ep} = 1.06$), the sunspot semi-distance was reduced to the minimum value of the possible range estimated from the observations, $L = 0.4$, leaving the other parameters of the equilibrium unchanged. No reduction of the minimum height for instability was found, which must be due to the strong stabilizing effect by the chosen shear field.

(6) Reconnection of the flux rope legs with the ambient field contributes only a minor part of the total rotation in our simulation series. It appears to remain weaker than the twist-driven rotation, or at most comparable, *i.e.*, considerably weaker than the shear-driven rotation. This can be seen most clearly in the 5π run with $B_{et} = 0$. Here the reconnection of the flux rope legs with the ambient field proceeds while the rope apex rises from $\approx 2\ h_0$ to $\approx 16\ h_0$, with the flux in the core of the rope being involved in the range of apex heights $h \sim (4\text{--}16)\ h_0$. However, the major part of the total rotation of $\approx 40°$ is already reached at low apex heights, $h \lesssim 5\ h_0$, *i.e.*, due to the helical kink mode. The apex height range during the reconnection of the flux rope legs in the shear-free 3.5π run is similar to the 5π run. The rotation profile of this run in Figure 6 shows about equal amounts of rotation in the height ranges $h \lesssim 5\ h_0$ and $h \sim (5\text{--}16)\ h_0$, indicating that the reconnection-driven rotation could here be comparable to the twist-driven rotation. Again, both remain considerably smaller than the rotation due to the shear in the 3.5π run that best fits the observation data.

These conclusions are also supported by the fact that the angular distance between the initial and new footpoints of the flux rope's magnetic axis, measured from $\mathbf{x} = 0$, remains far smaller than the total rotation of the rope (see the right panels in Figures 3–5).
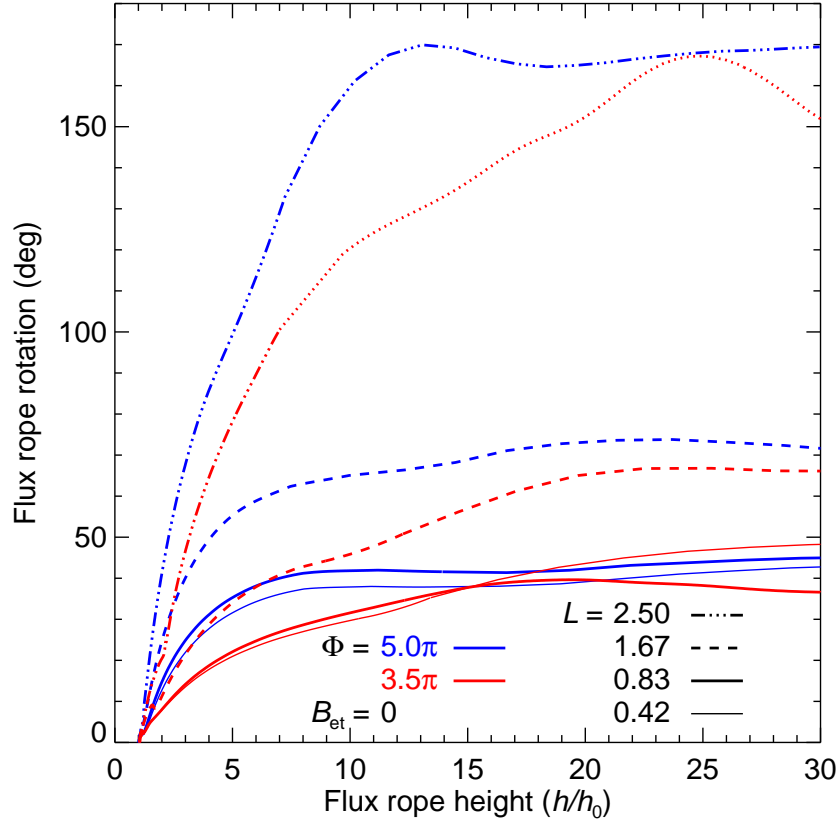
Figure 7. Dependence of flux rope rotation *vs.* height upon the distance L of the main flux concentrations in the source region from the PIL. Kink-unstable flux ropes ($\Phi = 5\pi$ and 3.5π) are considered for vanishing external shear field component, $B_{\mathrm{et}} = 0$.

3.2. Influence of the External Poloidal Field

The height profile of the poloidal field which is due to sources external to the flux rope, B_{ep}, is a further factor of potentially strong influence on the rotation. Erupting flux ropes rotate more strongly at low heights if the external field initially overlying the flux rope decreases more gradually with increasing height (Török, Berger, and Kliem, 2010). The relaxation of the magnetic tension in the erupting flux rope by rotation is then more pronounced because the relaxation by upward expansion is hindered, at least initially. The relevant length scale, $l_z = -[\mathrm{d}(\log B_{\mathrm{ep}})/\mathrm{d}z]^{-1}$, increases with increasing distance between the sources of B_{ep}, *i.e.*, between the main flux concentrations to the sides of the PIL. This can easily be seen for the Titov-Démoulin equilibrium, where this scale height is $l_z = (z + d)[1 + L^2/(z + d)^2]/3$.

Figure 7 shows that this effect remains weak as long as the distance between the sources of B_{ep}, $2L$, is smaller than distance between the footpoints of the erupting flux rope, $2D_{\mathrm{f}}$, but that it becomes very strong when the reverse relation holds. Here the sunspot semi-distance L is varied for the 5π and 3.5π runs

with no external shear field, $B_{\mathrm{et}} = 0$, to be 0.5, 1, 2, and 3 times the value estimated from the observations and used in Section 3.1 (Figures 3–6). The two distances are nearly equal if L is set to twice the estimated value. This is larger than the maximum of the range for L compatible with the observations (see the Introduction). Hence, the conclusions drawn from the series of simulations shown in Figure 6 are not sensitive to the actual value of the parameter L as long as it remains within this range. In particular, an external shear field component of strength close to the optimum values given in this figure is then required to reach the observed rotation.

Rotations even exceeding those produced mainly by the shear field in Figure 6 are achieved in the absence of a shear field for both twists if L exceeds D_{f} by a factor $\gtrsim 1.5$. A similar situation was realized in simulations of erupting flux ropes in Fan and Gibson (2003) and Gibson and Fan (2008), which showed strong rotations of 115–120 degrees with $B_{\mathrm{et}} = 0$. However, such large distances of the main polarities, relative to the length of the PIL and a filament channel between them, do not typically occur in fully developed active regions. Hence, the effect of a shear field (Isenberg and Forbes, 2007) will typically be involved if erupting flux rotates by large angles of order 90° and more.

3.3. Rise Profile

The results of Sections 3.1–3.2 lead to the question whether the initial twist and the shear field in the source volume of the eruption can be further constrained individually, although their combined effect on the rotation is similar. The rotation profile obviously is a powerful new diagnostic of the evolution of flux ropes in CMEs, however, for the considered event it does not allow to discriminate between the strongly and weakly kink-unstable cases shown in Figures 3 and 4, respectively. Therefore, we now consider the rise (time-height) profile of the erupting flux. This function reflects the growth rate of the instability driving the eruption. The growth rate varies strongly with the twist if this parameter exceeds the threshold of the helical kink mode (see, *e.g.*, Figure 5 in Török, Kliem, and Titov, 2004). When the variation of the twist is combined with a variation of the shear field strength in the opposite direction (one increasing, the other decreasing), such that the rotation profile stays nearly unchanged, then the rise profile will change even stronger: decreasing (increasing) shear field strength leads to higher (lower) KI growth rate. Thus, the combined comparison can constrain these parameters individually.

In order to compare the simulated rise profiles with the observed one, the time unit in the simulations, τ_A, must also be scaled to a dimensional value. Since $\tau_A = h_0/V_{\mathrm{A0}}$ and h_0 is already scaled, this is equivalent to adopting a value for the initial Alfvén velocity V_{A0} in the body of the prominence. So far, this parameter can hardly be derived from observations, since both the field and density structure of prominences are generally only poorly known. Therefore, here we work backwards by first finding the best match between the simulated and observed rise profiles and then checking whether the implied Alfvén velocity falls within an acceptable range. Lower bounds on the Alfvén velocity in filaments have been obtained through the application of seismological techniques to six
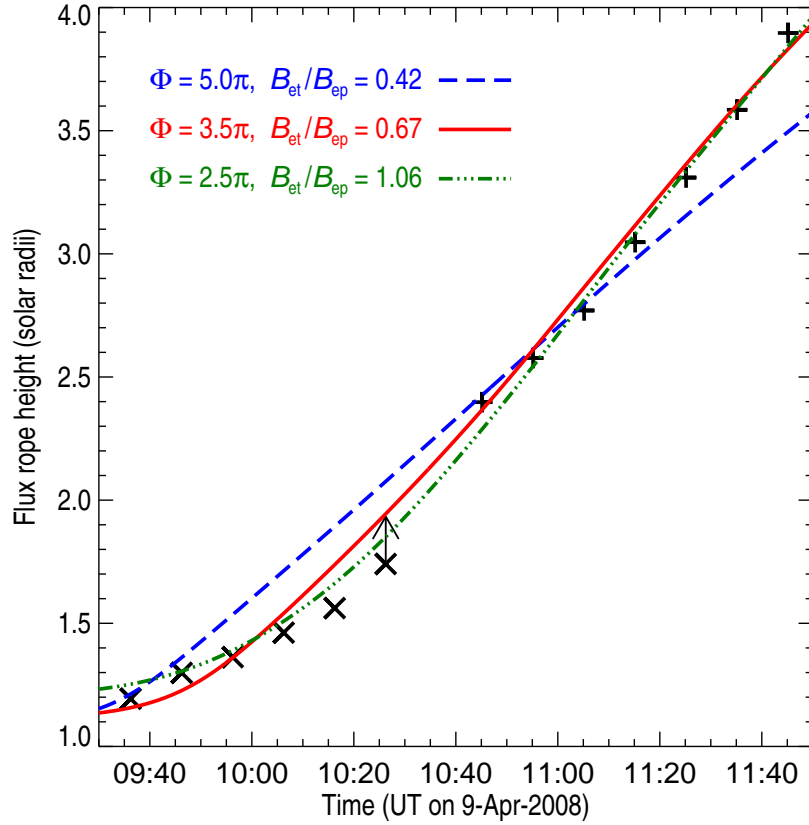
Figure 8. Comparison of the observed and simulated rise profiles of the flux rope apex, using the same scaling of lengths in the simulations as in Figure 6 and a start time of the eruption at 08:48:00 UT. EUVI and COR1 data from Paper I are plotted using the same symbols as in Figure 6. The 5π, 3.5π, and 2.5π runs of Figures 3–5 are scaled to these data assuming Alfvén velocities $V_{A0} = 420$ km s^{-1}, 550 km s^{-1}, and 560 km s^{-1}, respectively.

cases of oscillating filament threads (Terradas *et al.*, 2008). Five of these lie in the range $\sim (300–600)$ km s^{-1} if the length of the field lines that pass through the threads is assumed to be ~ 175 Mm, the length of the erupting structure estimated in Paper I. An upper bound of order 1000 km s^{-1} is widely accepted for old, dispersed active regions like the one considered here.

The rise profiles of the simulation runs shown in Figures 3–5 are scaled and matched to the observed profile in Figure 8. In selecting the scaling parameters for the best match, we adopt a start time of the eruption a couple of minutes before 08:51 UT, as estimated in Paper I. The conclusions drawn from the comparison do not depend upon the particular start time if chosen in this range. The value 08:48 UT used in Figure 8 yields the best match of the 3.5π and 2.5π runs with the observations and lies very close to (30 sec before) the last EUVI image prior to the occurrence of motions in the prominence along the path of the CME. Also, we give relatively low priority to the EUVI height data after 10 UT, since these may be smaller than the true heights, as discussed in Paper I.

The scaled rise profile of the simulation with $\Phi = 3.5\pi$ is found to fit the data quite well if the Alfvén velocity is chosen in the range $V_{A0} = (540$–$560)$ km s^{-1} and the start time of the simulation is placed in the range 08:45–08:50 UT (with the earlier time corresponding to the lower V_{A0}). These values appear very plausible.

We did not succeed to find a satisfactory fit by the higher twisted case. The corresponding curve in Figure 8 demonstrates this, using the same start time as for the 3.5π run and $V_{A0} = 420$ km s^{-1}. Increasing (decreasing) V_{A0} leads to a steeper (flatter) fit curve, *i.e.*, to a better fit at the larger (smaller) heights (if the start time is adjusted simultaneously), but it is obvious that the curve can never fit the combined EUVI and COR1 time-height data. Here the phase of accelerated rise ends too early because the instability grows and saturates too quickly. The rise profile of this simulation can be stretched on the time axis and formally be fit to the data if in addition to an unrealistically low Alfvén velocity of 300 km s^{-1} (lower than the terminal speed of the CME core) an unrealistically large extension of the prominence flux of 360 Mm (twice as large as the estimate in Paper I) are assumed. Both are not acceptable. This comparison with the data thus argues clearly against the occurrence of high twist and a strong helical kink instability in the considered event, in spite of the high total rotation.

Assuming the same start time as for the other two runs, the kink-stable low-twist case ($\Phi = 2.5\pi$) allows an acceptable approximation of the observed rise profile, which yields a plausible value of 560 km s^{-1} for the Alfvén velocity. The match is slightly worse in comparison to the 3.5π run because the curve does not reach the height of the first COR1 data point. Reducing V_{A0}, and adjusting the start time, allows for a nearly perfect match of the COR1 data, similar to the 3.5π run, but this moves the simulation curve, which already runs above all EUVI data points, further away from the measurements in this height range, so that the overall match is degraded.

The origin of the difference lies in the tendency of the torus instability to spread the main upward acceleration of the flux across a larger height range than the helical kink instability, which can be clearly seen in Figure 8. The height range for the torus instability is small only if the field in the source volume of the eruption decreases very rapidly with distance from the flux rope position (see Figure 1 in Kliem and Török, 2006), *i.e.*, in very compact active regions of high field strength, especially in quadrupolar ones. Since AR 10989 was already rather diffuse by the time of the eruption, there is no justification to make the initial configuration in the simulations more compact for a better fit of the rise profile by the kink-stable configuration.

3.4. Implications for the 9 April 2008 Eruption

Based on the good quantitative agreement of the simulated rotation and rise profiles with the observations, Sections 3.1–3.3 yield the following picture. The rotation profile in the height range $h \lesssim 20\, h_0 \approx 1.5\, R_\odot$ above the photosphere is well matched by a strongly kink-unstable case ($\Phi = 5\pi$), a weakly kink-unstable case ($\Phi = 3.5\pi$), and a kink-stable case ($\Phi = 2.5\pi$) if a shear field of appropriate strength is included in each of them. At greater heights, $h \approx$
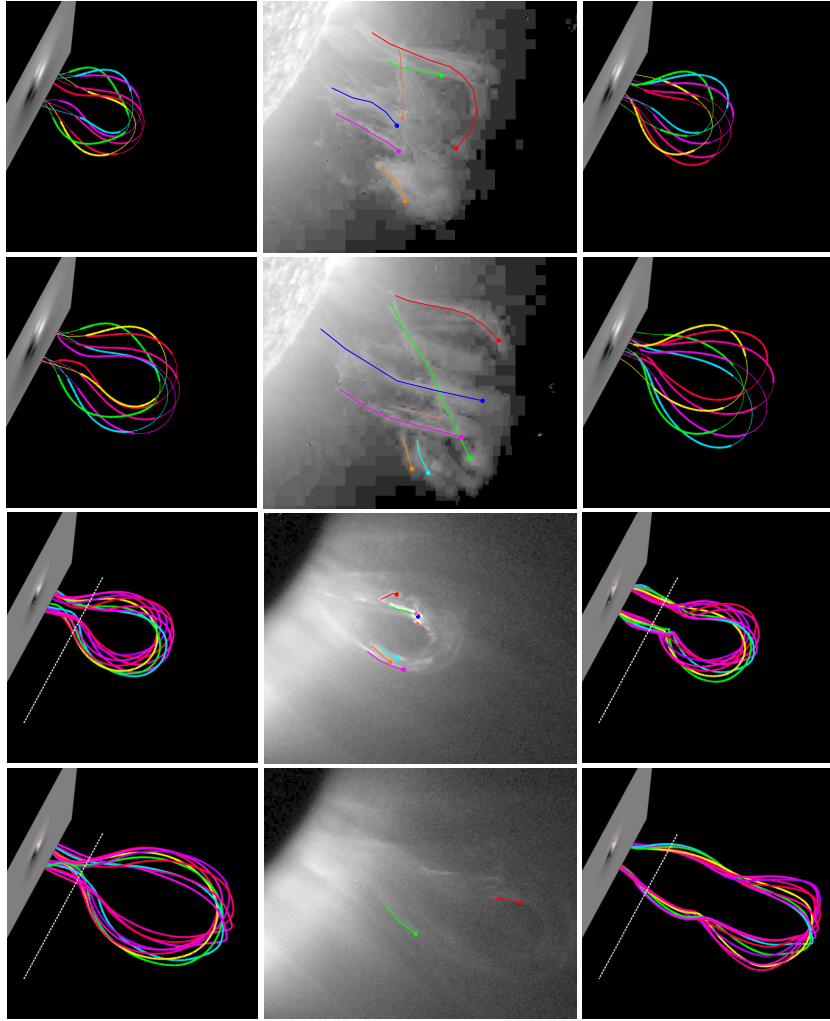
Figure 9. Comparison of simulated and observed flux rope shape for the kink-stable run ($\Phi = 2.5\pi$, $B_{\mathrm{et}}/B_{\mathrm{ep}} = 1.06$; left panels) and the weakly kink-unstable run ($\Phi = 3.5\pi$, $B_{\mathrm{et}}/B_{\mathrm{ep}} = 0.67$; right panels) in our parametric search which best match the observed rotation and rise profiles in their entirety. The STEREO images from Figure 1 are supplemented by an additional image at 10:26 UT from Paper I. For both runs, some experimenting with the field line selection was performed until also the observed shape was matched best. This yielded a flux bundle running slightly under the apex point of the rope's magnetic axis for the kink-stable run, as in Figure 5, and a flux bundle enclosing the axis for the kink-unstable run.

(20–30) $h_0 \approx (1.5$–$2.3)\ R_\odot$, the comparison yields a clear indication against the kink-stable case, which enters this range with an accelerated rotation, while the observed rotation levels off. The kink-stable case also requires a considerably stronger initial perturbation, lifting the flux rope apex into the torus-unstable range of heights, *i.e.*, to $h \gtrsim 2.6\ h_0 = 0.2\ R_\odot$, a value not supported by the observations. In comparison, the accelerated rise of the kink-unstable cases in

our simulation series starts essentially from $h_0 = 0.077\ R_\odot$, relatively close to the observed onset height of $(0.05–0.06)\ R_\odot$. The shear field required by the kink-stable case is comparable to the external poloidal field, $B_{\rm et}/B_{\rm ep} = 1.06$. In a bipolar region, this corresponds to a similar distance between the main polarities along and across the PIL, which is not supported by AR 10989 as long as its magnetic structure could be discerned in the approach to the limb (see Figure 4 in Paper I). The rise profile rules out the strongly kink-unstable case and yields a further indication against the kink-stable case, albeit only a weak one. Both the observed shape of the flux rope as a whole and the observed angles between individual threads and the rope axis can be approximately reproduced by all three model systems, but the overall match is best for the weakly kink-unstable case (Figures 3–5). This is substantiated by Figure 9, where we plot the sets of field lines for this and for the kink-stable case which were found to match the observations closest, out of many different sets that were considered.

The shape of the erupting flux rope's magnetic axis in the considered event is not sufficiently well defined by the observations to allow a clear discrimination between the three considered cases based on this property alone. Note that for other events it has proven to be decisive. For example, the shape of the two erupting filaments modeled in Török and Kliem (2005) could be matched only if an initial average twist of 5π was assumed, not with a twist of 4π.

Overall, we conclude that both strongly kink-unstable and kink-stable configurations can be excluded with a high degree of certainty, leaving a weakly kink-unstable initial configuration as the most likely source of the Cartwheel event. This configuration allows to reproduce the event with observationally supported values for several key parameters (flux rope length, distance of the main flux concentrations, initial orientation) and with plausible assumptions for the magnetic structure (flux rope in a simple bipolar active region) and for the remaining free parameters (twist and shear field strength).

Regardless of how definite the rejection of the other two cases is considered to be, the rotation of the erupting flux was primarily caused by a shear field (Isenberg and Forbes, 2007). Weaker contributions came from the relaxation of twist (most likely by a weak helical kink instability) and from reconnection with the ambient field.

4. Discussion

The major simplifying assumptions adopted for the modeling in this paper include (1) the neglect of the initial mainly axial propagation of the prominence, (2) the neglect of any asymmetry and complexity introduced by the large-scale overlying field, and (3) the assumption of a well defined, coherent flux rope (*i.e.*, the Titov-Démoulin model). We discuss these here to assess their potential influence on the results.

While the initial propagation of the prominence introduced an asymmetry and, therefore, definitely had the potential to produce some rotation, we expect that it could not contribute strongly because the propagation was approximately along the flux holding the prominence. This does not principally change the

magnetic configuration and the Lorentz forces which dominate the acceleration of plasma in the low-beta corona.

The effects belonging to category (2) are likely to be relevant primarily at considerable heights. AR 10989 was a relatively isolated region of simple, bipolar structure, and this holds also for its dispersed phase as long as it could be followed in the approach to the limb. The potential-field source-surface extrapolation of the photospheric field in Paper I shows that the large-scale coronal field associated with the polar fields and the heliospheric current sheet began to dominate already at heights $h \gtrsim 0.3\ R_\odot$ above the photosphere, where the horizontal field direction nearly reversed. The force by the field component along the line between the flux rope legs pointed in the direction of a clockwise rotation above this height, opposite to the force low in the corona. However, the shear field above $\sim 0.3\ R_\odot$ was weaker than the shear field in the core of the active region by more than an order of magnitude, so that it could efficiently counteract the continuing, oppositely directed force by the shear field at low heights, and the angular momentum of the already rotating flux rope, only by acting across a considerably larger height range. This is consistent with the fact that the possible weak reverse rotation occurred only at $h > 1.5\ R_\odot$ above the photosphere. Thus, the rotation caused by the shear field and twist inside the bipolar active region (at $h < 0.3\ R_\odot$) must have been dominant factors for the rotation in the height range up to $\sim 1.5\ R_\odot$ modeled here. We cannot exclude that the saturation of the rotation would have occurred at a greater height if the horizontal field had not changed its direction above the active region, however, this weakens only one of the three main arguments against the kink-stable configuration summarized in Section 3.4. The saturation of the rotation profile, at a very similar height, was also seen in another erupting quiescent filament (Bemporad, Mierla, and Tripathi, 2011; see their Figure 5).

The effect of the heliospheric current sheet is expected to become important only at even larger heights. Otherwise, the rotation would not have shown the saturation near $h \sim 1.5\ R_\odot$ and the possible subsequent slight reverse rotation; rather the continuation of the rotation to the value of $\approx 150°$ found at $13\ R_\odot$ would have proceeded already in the COR1 height range.

The assumption that erupting flux in CMEs takes the structure of a flux rope is strongly supported by all available observations. Quantitative differences to our modeling must occur when initial flux ropes of different structure are used. These are not likely to be substantial if only details of the structure differ. The helical kink mode is known to not overly depend on the details of the current channel's radial structure. This can be seen, for example, from the similar instability thresholds found in Mikic, Schnack, and van Hoven (1990), Baty and Heyvaerts (1996), Török, Kliem, and Titov (2004), and Fan and Gibson (2003) although flux ropes with and without a net current and with straight and arched geometries were investigated. Flux ropes with hollow current channels have recently been found to be representative of filament channels which have undergone substantial amounts of flux cancelation (*e.g.*, Su *et al.*, 2011). It is conceivable that their less compact current distribution leads to smaller rotations than the Titov-Démoulin equilibrium with the same twist. This will be a subject of future study. On the other hand, we believe that a strongly kink-unstable configuration of this

type would likely still not match the observed rise profile. The structure and strength of the external poloidal and toroidal field components do not depend upon the details of the flux rope structure, so that two aguments against the kink-stable configuration, which are based on the required initial lifting and on the ratio of B_{et} and B_{ep}, would likely still apply.

An overlying current sheet (Birn, Forbes, and Schindler, 2003) may be of stronger influence, but we have argued above that this was not the case for the considered event at the low coronal heights modeled in this paper.

The situation likely changes if the flux rope is far less coherent than the Titov-Démoulin configuration (Green, Kliem, and Wallace, 2011), especially if it is split (Bobra, van Ballegooijen, and DeLuca, 2008). The investigation how such complex cases might change our conclusions must be left for future work.

The comparison of the flux rope rotations found in this paper with the rotation in the simulation of a breakout CME by Lynch *et al.* (2009) suggests a strong dependence upon the existence of a flux rope at the onset of the eruption. In that simulation, the inflating flux of a continuously sheared arcade did not show any significant rotation up to a heliocentric height of $\approx 2\ R_\odot$. Flare reconnection commenced at this point, which progressively transformed the inner part of the arcade into a growing flux rope. The flux rope immediately began to rotate. This process was monitored until the core of the rope reached a heliocentric height of $\approx 3.5\ R_\odot$. Throughout this range, the rope showed a linear increase of its rotation angle with height, and the twist in the rope stayed below the threshold of the helical kink mode. The addition of poloidal flux by flare reconnection was largely complete in the middle of the height interval. The rotation profile in this model differs principally from the data presented here, even if only the height range $> 2\ R_\odot$ is considered, where a flux rope did exist. This suggests that the presence of a flux rope at the onset of the eruption was a key feature of the Cartwheel event.

An interesting result of our parametric study is that the erupting flux rope did always show some amount of rotation, even in the shear-free, kink-stable case included in Figure 6. We expect this to be generally valid if coherent force-free flux ropes are considered as the initial condition, because such ropes always possess twist. An untwisted flux tube, known as a Theta pinch, requires a radial pressure gradient to attain equilibrium. This is not available if the plasma beta is very small, as expected for the lower coronal part of active regions. Whether the observations support the occurrence of rotation in essentially all events does not yet seem to be clear. For example, Muglach, Wang, and Kliem (2009) report that only about 10 cases of unambiguous rotation in erupting filaments not very far from Sun center could be identified in the EUV observations by the EIT instrument (Delaboudinière *et al.*, 1995) for the whole solar cycle 23. However, many cases of only moderate rotation may remain undetected in such data, due to the projection in the plane of the sky. Yurchyshyn, Abramenko, and Tripathi (2009) report 101 partial and full halo CMEs which show a very broad distribution of the difference between the estimated initial and final orientations at distances up to 30 $R_\odot$; these angles do not show a clustering at zero degrees. However, they represent the net effect of rotation in the corona and in the inner solar wind where the heliospheric current sheet likely dominates. If the fraction of

non-rotating events is relatively small, then a plausible explanation is that other processes counteract the rotation by twist relaxation and the shear field in these cases, for example reconnection with the ambient field. If the fraction is large, then such nearly exact cancelation of rotations is unlikely to be the primary explanation. The implication would then be that the current distribution in the erupting field is often less compact or less coherent than in the Titov-Démoulin flux rope, including the possibility that a flux rope does not yet exist at the onset of the eruption.

5. Conclusions

Our parametric study of force-free flux ropes which erupt from simple bipolar source regions with no overlying current sheet and rotate about the direction of ascent yields the following conclusions.

1) Both the force by an external shear field component B_{et} (Isenberg and Forbes, 2007) and the relaxation of twist Φ (*e.g.*, Török, Berger, and Kliem, 2010), are potentially very significant contributors to the rotation.

2) For parameters typical of CME source regions, in particular if the sources of the external stabilizing field (usually the main flux concentrations next to the PIL) have a smaller distance than the footpoints of the erupting flux, the shear field yields the dominant contribution to the rotation for a wide range of shear field strengths. The relaxation of twist remains the weaker contributor under these conditions, even if it is sufficiently high to trigger the helical kink instability. However, since twist always exists in force-free flux ropes, it always causes at least some rotation. Strong rotations ($\gtrsim 90°$) can be produced by the twist alone, but only for considerably larger distances between the sources of the external stabilizing field than typically observed.

3) The rotation in low-beta plasma is not guided by the changing orientation of the PIL with height. For the geometrical conditions typical of CME source regions, it is opposite in direction (see the Appendix).

4) For a given chirality of the configuration, the external shear field and the twist cause flux rope rotation in the same direction, which is clockwise for right-handed field and counterclockwise for left-handed field if seen from above.

5) The two processes are related to each other when considered in terms of magnetic helicity. Both convert initial twist helicity of the flux rope into writhe helicity. The same total rotation, and rotation profiles which are very similar in a substantial part of the total height range of rotation, result in a range of B_{et}–Φ combinations.

6) The rotation due to twist relaxation tends to act mainly low in the corona, in a height range up to only a few times the distance between the footpoints of the erupting flux. The rotation by the shear field tends to be distributed across a larger height range.

7) The mere fact that erupting flux rotates does not by itself imply that the helical kink instability occurred.

8) The relative contributions to the total rotation by the shear field and by the twist can be disentangled by comparing both the observed rotation and rise

profiles with the corresponding curves from a model, since these profiles possess a different dependence upon the B_{et}–Φ parameter combination. The resulting estimate for the twist allows one to judge the occurrence of the helical kink instability.

9) Magnetic reconnection contributes only weakly (much less than the shear field) to the total rotation in the simple bipolar source regions considered.

From the comparison with the simulation of rotating flux in Lynch *et al.* (2009) we conclude:

10) The rotation profile differs strongly between configurations with and without a flux rope at the onset of the eruption.

The comparison with the stereoscopic observations and three-dimensional reconstruction of the erupting prominence in the 9 April 2008 "Cartwheel CME" additionally shows the following.

11) The rotation profile obtained in Paper I from the stereoscopic reconstruction of STEREO data is equally well reproduced by our model up to heights $\approx 1.5\ R_{\odot}$ above the photosphere for a range of Φ–B_{et} combinations which include a strongly kink-unstable case ($\Phi = 5\pi$, $B_{et}/B_{ep} = 0.42$), a weakly kink-unstable case ($\Phi = 3.5\pi$, $B_{et}/B_{ep} = 0.67$), and a kink-stable case ($\Phi = 2.5\pi$, $B_{et}/B_{ep} = 1.06$). However, the strongly kink-unstable configuration is ruled out by the simultaneous consideration of the rise profile, and several features of the kink-stable model argue strongly against this configuration. These are the implied high value of the shear field, the rotation profile at greater heights, and the unrealistic start height of the unstable rise of $\approx 0.2\ R_{\odot}$. Hence, the occurrence of a weak helical kink instability in the Cartwheel event is very likely.

Our results add to the complexity of the phenomenon of flux rope rotation in eruptions which is already known from investigations that focused on the influence of reconnection (*e.g.*, Jacobs *et al.*, 2009; Shiota *et al.*, 2010; Cohen *et al.*, 2010; Thompson, 2011; Lugaz *et al.*, 2011). An overall very complicated dependence on several parameters and on the structure of the ambient field is revealed. Thus, the quantitative prediction of the rotation is a difficult task. The parametric study performed here indicates for simple bipolar source regions that the strength of the external shear field is the primary parameter determining the total rotation. The twist and the height profile of the external poloidal field are of relatively minor importance as long as they stay in the typical ranges indicated by the observations. We did not yet study a possible influence of the height profile of the external shear field. The external shear field of filament channels may be estimated to sufficient precision from a simple linear force-free field extrapolation. It will be worth testing whether numerical modeling starting from such fields, embedded in current-free outer field, yields rotations in agreement with observations of eruptions from bipolar source regions.

Several investigations indicate that erupting flux ropes align with the heliospheric current sheet in the course of their interplanetary propagation (*e.g.*, Bothmer and Schwenn, 1998; Yurchyshyn, 2008; Paper I). This suggests that the coronal rotation merely decides whether a parallel or an antiparallel alignment
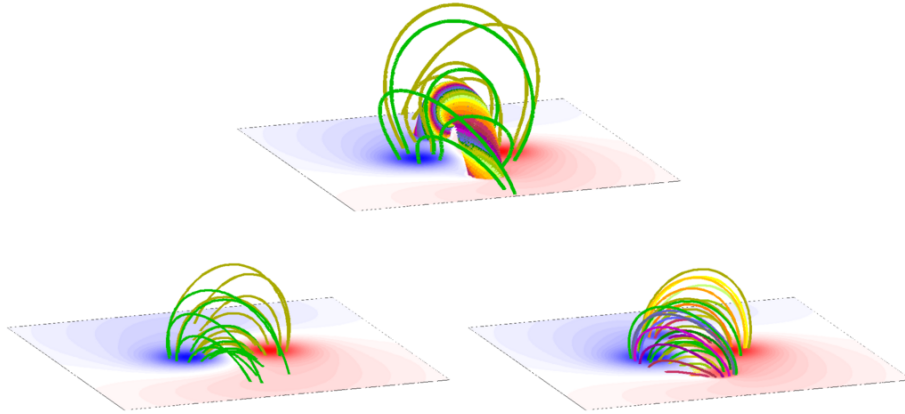
Figure 10. Visualization of the weakly kink-unstable modified Titov-Démoulin equilibrium ($\Phi = 3.5\pi$, $B_{\mathrm{et}}/B_{\mathrm{ep}} = 0.67$; Figures 2 and 4) whose eruption characteristics match the observations of the Cartwheel CME best (top panel) and of the corresponding external field (bottom left) and potential field (bottom right). The magnetogram and field lines starting in the photospheric flux concentrations are shown.

will result at 1 AU. However, since complex physics is involved and since rotations on the order of 90° may not be rare, the quantitative study of the effects that determine the rotation in the corona remains of high scientific and practical interest.

Appendix

There are quite strong indications that CMEs align with the heliospheric current sheet in the course of their propagation, *i.e.*, with the PIL in the solar wind (see references in Section 5). This leads to the question whether the PIL guides the rotation of erupting flux ropes also in the corona. Here the PIL formed by the external field, due to sources outside the flux rope, must be considered. We use "CPIL" to denote this structure in the corona, where $\beta < 1$. The heliospheric current sheet and the CPIL differ in two properties of relevance here. First, in the solar wind $\beta > 1$, so that the pressure gradient is generally dominant over the Lorentz force, while the opposite is true in the corona. Second, the heliospheric current sheet is the location of pressure gradients and Lorentz forces, while the CPIL generally lacks both. In the low-beta corona, currents are induced at separatrix surfaces, or at quasi separatrix layers, if the equilibrium is perturbed or lost. The CPIL generally does not coincide with these structures. Therefore, the CPIL should not influence the rotation of erupting flux ropes in this height range.

Figure 10 shows the initial equilibrium of the weakly kink-unstable run which matches the Cartwheel event best, the corresponding external field, and the potential field that results when the full magnetogram of the vertical field component of the equilibrium, $B_z(x, y, 0)$, is extrapolated into the volume above. The
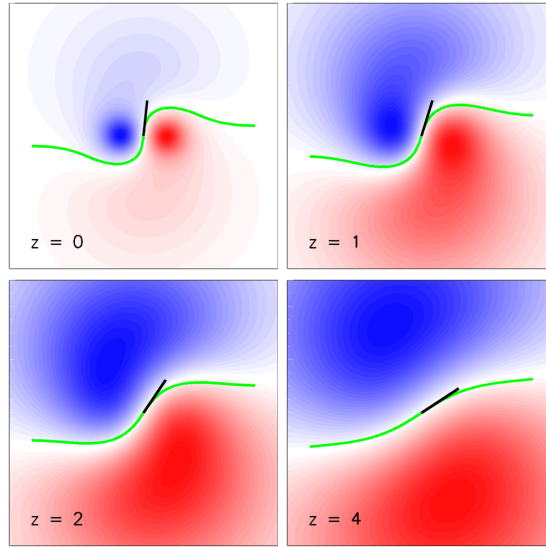
Figure 11. Orientation of the PIL in the external field of the configuration shown in Figure 10 at the position of the flux rope and different heights. The orientation is indicated by a black line.
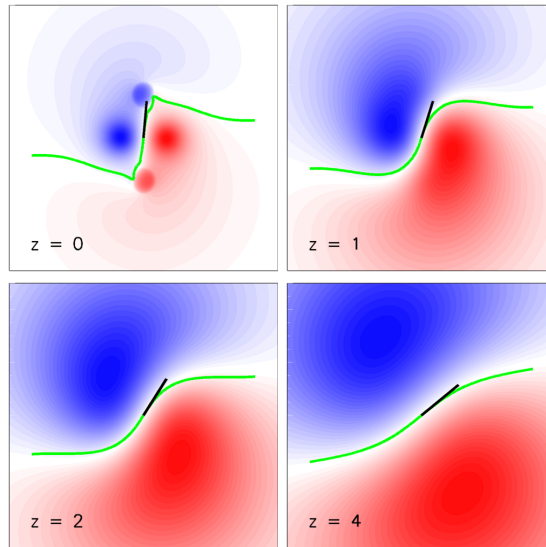
Figure 12. Same as Figure 11 for the potential field of the configuration shown in Figure 10.

full magnetogram includes the contributions from the flux rope, which are excluded from the external field. The CPIL of this configuration at the photospheric and three coronal levels is shown in Figure 11. The CPIL changes its orientation in a clockwise sense if one goes upward, but the unstable flux rope rotates in a counterclockwise direction, since it is left handed. The clockwise changing CPIL orientation results from the dominance of the external toroidal field, B_{et}, over

the external poloidal field, B_{ep}, at great heights. This situation can typically be expected to occur because B_{et} typically has a larger spatial scale than B_{ep} (set by the distance between the sources in the photosphere). The important fact here is that the CPIL does not appear to have any significant influence on the rotation of the flux rope in the zero-beta simulations performed in this paper. For the reasons given above, this is valid also if other height profiles of B_{et} or B_{ep} lead to a different profile of the CPIL orientation with height.

Finally, we consider the approximation of the true CPIL by the PIL in a potential-field extrapolation of the full photospheric magnetogram, $B_z(x, y, 0)$. In practice, it is difficult or even impossible to determine the external field. This requires the determination of the coronal currents through a nonlinear force-free extrapolation from a vector magnetogram. The former is still difficult to carry out and the latter may not be available. The PIL in the potential field extrapolated from the magnetogram of the weakly kink-unstable configuration in Figure 10 is shown in Figure 12. Its orientation *vs.* height is very similar to the behavior of the true CPIL. This supports the conclusions drawn in Paper I from a potential-field source-surface extrapolation for the source region of the Cartwheel CME.

References

Amari, T., Aly, J., Mikic, Z., Linker, J.: 2010, *Astrophys. J. Lett.* **717**, 26.
Aulanier, G., Török, T., Démoulin, P., DeLuca, E.E.: 2010, *Astrophys. J.* **708**, 314.
Baty, H., Heyvaerts, J.: 1996, *Astron. Astrophys.* **308**, 935.
Bemporad, A., Mierla, M., Tripathi, D.: 2011, *Astron. Astrophys.* **531**, A147.
Birn, J., Forbes, T.G., Schindler, K.: 2003, *Astrophys. J.* **588**, 578.
Bobra, M.G., van Ballegooijen, A.A., DeLuca, E.E.: 2008, *Astrophys. J.* **672**, 1209.
Bothmer, V., Schwenn, R.: 1998, *Annales Geophysicae* **16**, 1.
Chen, P.F., Shibata, K.: 2000, *Astrophys. J.* **545**, 524.
Cohen, O., Attrill, G.D.R., Schwadron, N.A., Crooker, N.U., Owens, M.J., Downs, C., Gombosi, T.I.: 2010, *J. Geophys. Res.* **115**(A14), 10104.
Delaboudinière, J., Artzner, G.E., Brunaud, J., Gabriel, A.H., Hochedez, J.F., Millier, F., Song, X.Y., Au, B., Dere, K.P., Howard, R.A., Kreplin, R., Michels, D.J., Moses, J.D., Defise, J.M., Jamar, C., Rochus, P., Chauvineau, J.P., Marioge, J.P., Catura, R.C., Lemen, J.R., Shing, L., Stern, R.A., Gurman, J.B., Neupert, W.M., Maucherat, A., Clette, F., Cugnon, P., van Dessel, E.L.: 1995, *Solar Phys.* **162**, 291.
Fan, Y., Gibson, S.E.: 2003, *Astrophys. J. Lett.* **589**, 105.
Gibson, S.E., Fan, Y.: 2008, *J. Geophys. Res.* **113**(A12), 9103.
Green, L.M., Kliem, B., Wallace, A.J.: 2011, *Astron. Astrophys.* **526**, A2.
Green, L.M., Kliem, B., Török, T., van Driel-Gesztelyi, L., Attrill, G.D.R.: 2007, *Solar Phys.* **246**, 365.
Howard, R.A., Moses, J.D., Vourlidas, A., Newmark, J.S., Socker, D.G., Plunkett, S.P., Korendyke, C.M., Cook, J.W., Hurley, A., Davila, J.M., Thompson, W.T., Cyr, O.C.S., Mentzell, E., Mehalick, K., Lemen, J.R., Wuelser, J.P., Duncan, D.W., Tarbell, T.D., Wolfson, C.J., Moore, A., Harrison, R.A., Waltham, N.R., Lang, J., Davis, C.J., Eyles,

    C.J., Mapson-Menard, H., Simnett, G.M., Halain, J.P., Defise, J.M., Mazy, E., Rochus, P., Mercier, R., Ravet, M.F., Delmotte, F., Auchere, F., Delaboudiniere, J.P., Bothmer, V., Deutsch, W., Wang, D., Rich, N., Cooper, S., Stephens, V., Maahs, G., Baugh, R., Mcmullin, D.: 2008, *Space Sci. Rev.* **136**, 67.

Isenberg, P.A., Forbes, T.G.: 2007, *Astrophys. J.* **670**, 1453.

Jacobs, C., Roussev, I.I., Lugaz, N., Poedts, S.: 2009, *Astrophys. J.* **695**, 171.

Kliem, B., Török, T.: 2006, *Phys. Rev. Lett.* **96**, 255002.

Kliem, B., Titov, V.S., Török, T.: 2004, *Astron. Astrophys.* **413**, 23.

Kliem, B., Linton, M.G., Török, T., Karlický, M.: 2010, *Solar Phys.* **266**, 91.

Landi, E., Raymond, J.C., Miralles, M.P., Hara, H.: 2010, *Astrophys. J.* **711**, 75.

Lugaz, N., Downs, C., Shibata, K., Roussev, I.I., Asai, A., Gombosi, T.I.: 2011, *Astrophys. J.* **738**, 127.

Lynch, B.J., Antiochos, S.K., Li, Y., Luhmann, J.G., DeVore, C.R.: 2009, *Astrophys. J.* **697**, 1918.

Martin, S.F.: 2003, *Advances in Space Research* **32**, 1883.

Mikic, Z., Linker, J.A.: 1994, *Astrophys. J.* **430**, 898.

Mikic, Z., Schnack, D.D., van Hoven, G.: 1990, *Astrophys. J.* **361**, 690.

Muglach, K., Wang, Y., Kliem, B.: 2009, *Astrophys. J.* **703**, 976.

Panasenco, O., Martin, S., Joshi, A.D., Srivastava, N.: 2011, *Journal of Atmospheric and Solar-Terrestrial Physics* **73**, 1129.

Patsourakos, S., Vourlidas, A.: 2011, *Astron. Astrophys.* **525**, A27.

Romano, P., Contarino, L., Zuccarello, F.: 2003, *Solar Phys.* **214**, 313.

Rust, D.M., Kumar, A.: 1996, *Astrophys. J. Lett.* **464**, L199.

Rust, D.M., LaBonte, B.J.: 2005, *Astrophys. J.* **622**, 69.

Sakurai, T.: 1976, *Publ. Astron. Soc. Japan* **28**, 177.

Shiota, D., Kusano, K., Miyoshi, T., Shibata, K.: 2010, *Astrophys. J.* **718**, 1305.

Su, Y., Surges, V., van Ballegooijen, A., DeLuca, E., Golub, L.: 2011, *Astrophys. J.* **734**, 53.

Terradas, J., Arregui, I., Oliver, R., Ballester, J.L.: 2008, *Astrophys. J.* **678**, 153.

Thompson, W.T.: 2011, *Journal of Atmospheric and Solar-Terrestrial Physics* **73**, 1138.

Thompson, W.T., Kliem, B., Toeroek, T.: 2009, In: *AAS/Solar Physics Division Meeting #40*, *AAS/Solar Physics Division Meeting* **40**, 21.11.

Thompson, W.T., Kliem, B., Török, T.: 2011, *Solar Phys.*. doi:10.1007/s11207-011-9868-5.

Titov, V.S., Démoulin, P.: 1999, *Astron. Astrophys.* **351**, 707.

Török, T., Kliem, B.: 2003, *Astron. Astrophys.* **406**, 1043.

Török, T., Kliem, B.: 2005, *Astrophys. J. Lett.* **630**, 97.

Török, T., Kliem, B.: 2007, *Astronomische Nachrichten* **328**, 743.

Török, T., Berger, M.A., Kliem, B.: 2010, *Astron. Astrophys.* **516**, A49.

Török, T., Kliem, B., Titov, V.S.: 2004, *Astron. Astrophys.* **413**, 27.

Vourlidas, A., Colaninno, R., Nieves-Chinchilla, T., Stenborg, G.: 2011, *Astrophys. J. Lett.* **733**, L23.

Williams, D.R., Török, T., Démoulin, P., van Driel-Gesztelyi, L., Kliem, B.: 2005, *Astrophys. J. Lett.* **628**, 163.

Yurchyshyn, V.: 2008, *Astrophys. J.* **675**, 49.

Yurchyshyn, V., Abramenko, V., Tripathi, D.: 2009, *Astrophys. J.* **705**, 426.